RESEARCH ARTICLE

NANO · MICRO small
www.small-journal.com

Protein Aggregation on Metal Oxides Governs Catalytic Activity and Cellular Uptake

Robert Nißler, Lena Dennebouy, Alexander Gogos, Lukas R.H. Gerken, Maximilian Dommke, Monika Zimmermann, Michael A. Pais, Anna L. Neuer, Martin T. Matter, Vera M. Kissling, Simone de Brot, Ioana Lese, and Inge K. Herrmann**

Engineering of catalytically active inorganic nanomaterials holds promising prospects for biomedicine. Catalytically active metal oxides show applications in enhancing wound healing but have also been employed to induce cell death in photodynamic or radiation therapy. Upon introduction into a biological system, nanomaterials are exposed to complex fluids, causing interaction and adsorption of ions and proteins. While protein corona formation on nanomaterials is acknowledged, its modulation of nanomaterial catalytic efficacy is less understood. In this study, proteomic analyses and nano-analytic methodologies quantify and characterize adsorbed proteins, correlating this protein layer with metal oxide catalytic activity in vitro and in vivo. The protein corona comprises up to 280 different proteins, constituting up to 38% by weight. Enhanced complement factors and other opsonins on nanocatalyst surfaces lead to their uptake into macrophages when applied topically, localizing >99% of the nanomaterials in tissue-resident macrophages. Initially, the formation of the protein corona significantly reduces the nanocatalysts' activity, but this activity can be partially recovered in endosomal conditions due to the proteolytic degradation of the corona. Overall, the research reveals the complex relationship between physisorbed proteins and the catalytic characteristics of specific metal oxide nanoparticles, providing design parameters for optimizing nanocatalysts in complex biological environments.

1. Introduction

Catalytically active inorganic nanomaterials have emerged as promising candidates for a spectrum of potential applications in biomedicine.[1–4] Specifically, enzyme-mimetic inorganic nanoparticles, commonly referred to as nanozymes, have demonstrated capabilities in augmenting wound healing,[5–8] mitigating ischemia/reperfusion injuries,[9,10] and hold great prospects for other therapeutic interventions.[11–13] One attribute of such nanozymes is their ability to mimic the functionalities of endogenous enzymes, such as catalase and sodium oxide dismutase (SOD) activity.[14] Intriguingly, inorganic nanozymes, in comparison to their organic analogs, may exhibit enhanced stability and extended longevity. Such nanozymes typically are composed of metal or metal oxides with a high surface-area-to-volume ratio. Beyond their recognized role in radical scavenging, metal oxides may also play pivotal roles in radical generation, particularly during treatments like

R. Nißler, L. Dennebouy, A. Gogos, L. R. Gerken, M. Zimmermann, A. L. Neuer, M. T. Matter, I. K. Herrmann
Nanoparticle Systems Engineering Laboratory, Institute of Energy and Process Engineering (IEPE), Department of Mechanical and Process Engineering (D-MAVT)
ETH Zurich
Sonneggstrasse 3, Zurich 8092, Switzerland
E-mail: rnissler@ethz.ch; ingeh@ethz.ch, inge.herrmann@empa.ch

The ORCID identification number(s) for the author(s) of this article can be found under https://doi.org/10.1002/smll.202311115

DOI: 10.1002/smll.202311115

R. Nißler, A. Gogos, L. R. Gerken, M. Zimmermann, A. L. Neuer, M. T. Matter, V. M. Kissling, I. K. Herrmann
Particles-Biology Interactions, Department of Materials Meet Life
Swiss Federal Laboratories for Materials Science and Technology (Empa)
Lerchenfeldstrasse 5, St. Gallen 9014, Switzerland

R. Nißler, I. K. Herrmann
The Ingenuity Lab, University Hospital Balgrist
University of Zurich
Forchstrasse 340, Zurich 8008, Switzerland

M. Dommke
Institute of Technical Chemistry and Environmental Chemistry
Friedrich Schiller University Jena
Philosophenweg 7a, 07743 Jena, Germany

M. A. Pais, I. Lese
Department of Plastic and Hand Surgery, Inselspital
Bern University Hospital
Bern 3010, Switzerland

photodynamic[15] and radiation therapy.[16] Indeed, recent research has demonstrated promising radical generation by photocatalytically active materials, such as TiO_2 and HfO_2 nanoparticles, in radiotherapy.[17–19] This is highlighted by the clinical approval of HfO_2 as NBTXR3/Hensify for the European market as treatment of locally advanced soft tissue sarcoma via intratumoral injection combined with photon radiotherapy.[3,20]

As with classical catalysis, understanding the intricacies of catalytic efficacy and potential site inhibition remains paramount also for nanozymes. This is accentuated considering the complex compartmental architecture of biological systems and the various chemical microenvironments. The activity of the prominent radical scavenger CeO_2 for instance relies on a unique redox chemistry, cycling between Ce^{3+} and Ce^{4+} states.[21] However, most biological systems exhibit fluids with high ionic strengths, enriched with a variety of salts, which can directly influence the catalytic activity of such nanomaterials. For example, phosphate has been identified as a potent inhibitor of the nanozyme activity of cerium oxide.[22] The underlying mechanism is the affinity of phosphate to bind with the catalytically active Ce^{3+} sites, leading to the formation of the highly stable, yet catalytically dormant, cerium phosphate on the nanomaterial's surface.[22] In addition to high salt contents, the majority of biological fluids contain proteins, albeit with varying concentrations and compositions. A well-established phenomenon is the rapid adherence of proteins to the surfaces of (inorganic) nanomaterials when exposed to protein-rich bodily fluids, which results in the formation of the protein corona.[23,24] The properties of this corona, in terms of its composition and dynamism, have been subjects of intensive research endeavors,[25] however, are strongly dependent on the nanoparticle (NP) properties such as surface charge, particle size, and shape.[26,27] Most interestingly, the specificity of protein-NP interactions leads to the accumulation of proteins mediating endocytosis, cell binding, or clearance by cells, overall influencing the nanomaterials in vivo destination.[23,25,28] Such factors can further act as opsonins or dysopsonins, mediating uptake by immune cells like macrophages, hence governing circulation times, targeting sites, and nanotoxicity in general.[29,30]

While the genesis of the protein corona is universally recognized, its effect on the catalytic activity of nanomaterials remains poorly understood. Yet, recent research highlights the profound influence of surface modifications and the neighboring macromolecules on the catalytic sites and activity.[31] These influences can be direct, as seen in radical scavenging, or manifest indirectly, for example, as diffusion impediments. The milieu of body fluids such as blood or seroma fluid alongside the distinct chemical composition of cellular organelles, especially those containing proteases, warrant in-depth exploration.

In this study, we investigated the role of the protein corona on the catalytic activity of inorganic nanomaterials, both as radical scavengers and radical generators. We investigated a portfolio of cerium and manganese-based inorganic nanozymes, alongside potent photocatalytically active radio-enhancers TiO_2 and HfO_2. Our explorations into the relationship between nanomaterials and proteins, underpinned by proteomic analyses, indicate that macrophage-oriented complement factors accumulated on the nanomaterial surface, effectively directing the nanoparticles to macrophages after topical application. Further, we quantified the impact of the protein corona on the enzymatic activity of the nanomaterials, and subsequently unveiled strategies to conserve this activity. Finally, we discerned that the enzymatic activity of nanozymes and radio-enhancers is recovered at the intracellular level, likely orchestrated by the proteases present within endo-/lysosomes.

2. Results and Discussion

2.1. Nanocatalyst Synthesis and Physicochemical Characterization

To investigate and compare various metal oxide-based nanocatalysts, each was synthesized using flame–spray-pyrolysis.[32] This method facilitates not only the synthesis of single-metal oxide nanoparticles but also the generation of mixed-metal oxide nanomaterials. By dissolving the metal–organic precursor in an organic solvent, the required elemental composition can be introduced into a CH_4/O_2 flame. The controlled combustion results in nanoparticle nucleation and formation within the flame. Subsequently, these nanoparticles can be collected on a glass-fiber filter mounted above the flame. This efficient synthesis process, apt for large-scale industrial production, provides nanoparticles as a sterile, dry powder without further purification needs. Consequently, metal oxide nanocatalysts were produced that had demonstrated radicals (reactive oxygen species, ROS) scavenging (CeO_2 and Mn_3O_4) and ROS generating (TiO_2 and HfO_2) capabilities. Moreover, Bioglass (bioactive glass, BG) a mixed metal oxide, that is typically utilized to improve soft and hard tissue regeneration and biocompatibility in general was included in the study.[33,34] Combining multiple types of nanomaterials can yield hybrids that unite advantages. For example, BG combined with SrO, Zn, and CeO_2, yields a hybrid material with antibacterial, anti-inflammatory, hemostatic, and ROS scavenging attributes that has been employed as a wound healing agent.[5,32,35] After synthesis, the nanoparticles were thoroughly characterized. ICP-OES elemental analysis confirmed the theoretical chemical composition of the mixed metal oxide nanoparticles (**Figure 1a**). X-ray diffractometry (XRD, Figure 1b) further corroborated the successful synthesis of all nanomaterials, aligning with the reference pattern used for Rietveld refinement. The calculated crystal sizes are in agreement with the primary particle size observed via transmission electron microscopy (TEM) (Figure 1c,d; Figure S1, Supporting Information). Figure 1c displays a representative TEM image of the CeO_2-BG hybrid as an example, showcasing electron-dense (black) CeO_2 particle agglomerates surrounded by the less dense (gray) BG matrix. The particle size distribution determined by TEM (Figure 1d) shows that HfO_2 is the smallest particle (3.6 nm) and Bioglass the largest (average size of 15.5 nm). These nanoparticles show characteristics typical for combustion-made particles, however, modulation of synthesis parameters enables engineering of the specific particle sizes and agglomeration state.[36] For the CeO_2–BG hybrid, the CeO_2 size is shown, whereas the BG matrix was similar in size to its undoped counterpart. The as-prepared nanomaterials can be

S. de Brot
COMPATH, Institute of Animal Pathology
University of Bern
Bern 3012, Switzerland

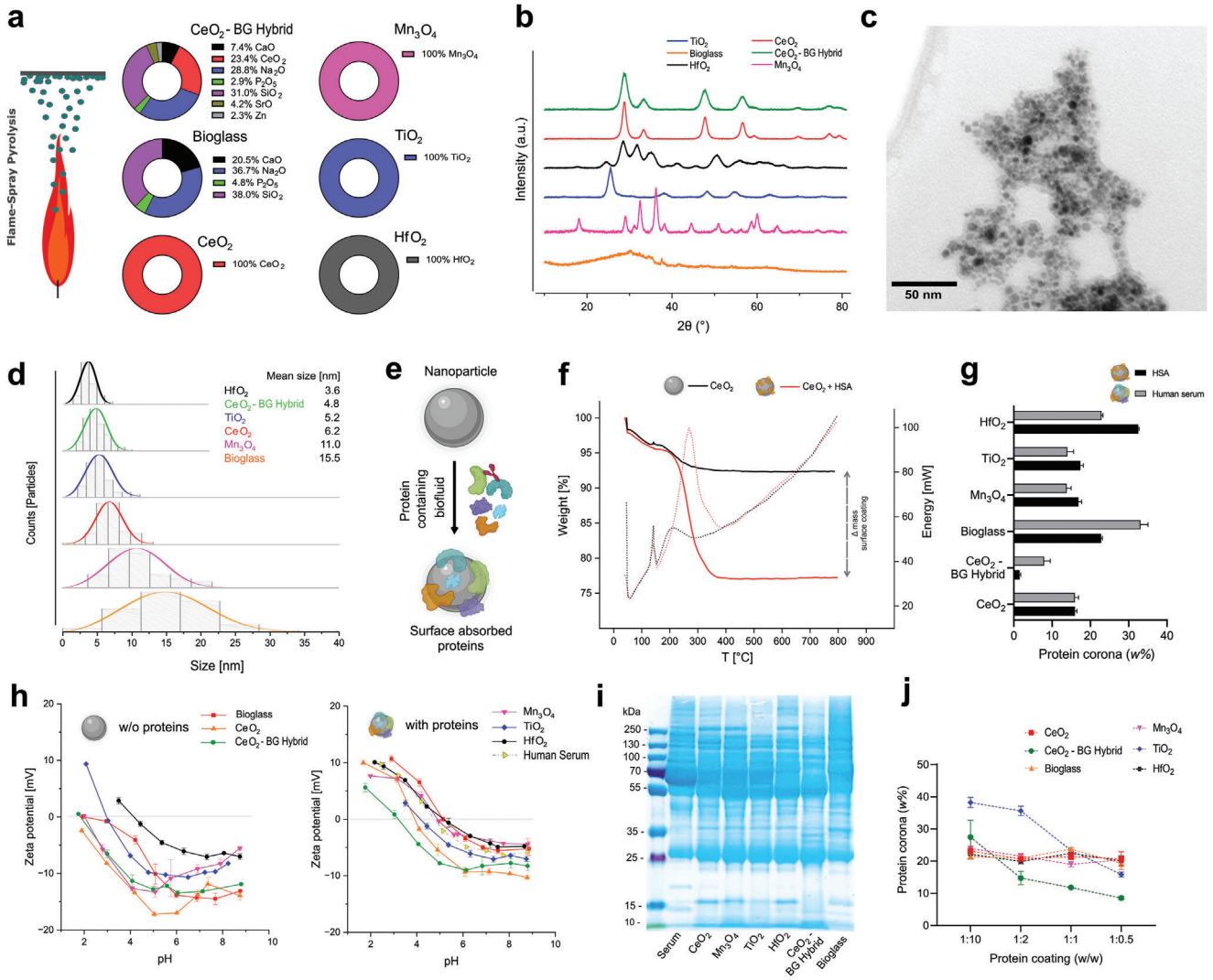

Figure 1. Protein aggregation of metal–oxide nanozymes. a) Metal–oxide nanoparticles were synthesized by flame–spray pyrolysis. The elemental composition of BG and CeO_2–Bioglass hybrid was determined by ICP-OES and displayed as oxides. b) XRD pattern of the six different metal–oxide nanoparticles. c) Exemplary TEM image of CeO_2–Bioglass hybrid nanoparticles with electron-dense CeO_2 particles and an amorphous Bioglass shell. d) Primary nanoparticle sizes obtained by TEM, shown as probability density function of the descriptive histograms (n ≈ 100 particles each). e) Schematic representation of nanoparticles interacting with a protein containing biofluid. f) TGA analysis of human serum albumin (HSA)-modified CeO_2 nanoparticles and their non-coated counterpart. The mass difference between both samples allows the quantification of the protein corona. g) Quantification of surface absorbed proteins (*w*%), after incubation with HSA and human serum in a ratio of 1 mg mL^{-1} NP to 1 mg mL^{-1} proteins (mean ± SD, $n = 3$). h) ζ-potential titration of uncoated (left) and serum protein (1:1, right) coated NPs show a drastic change in surface charge after interacting with proteins (in Ringer lactate buffer; mean ± SD, $n = 1$). i) Separation of the surface absorbed proteins from human serum by SDS-PAGE and visualization by Coomassie blue staining. j) Varying ratios of protein concentration to nanoparticle concentration for the initial coating results in increasing amounts of absorbed proteins for CeO_2–Bioglass hybrid and TiO_2 nanoparticles (1 mg mL^{-1} NP: X mg mL^{-1} proteins) (mean ± SD, $n = 3$).

immediately used for biomedical purposes, as discussed earlier.[6] When exposed to protein-rich biological fluids like blood, proteins aggregate on the NP surface, a phenomenon known as protein corona formation (Figure 1e). This prompts two crucial questions regarding i) the overall number of proteins that bind, as well as ii) the protein corona composition. The answers to these questions dictate the nanoparticles' biological fate and potential immune reactions.[25,27,28] To measure the amount of proteins bound to the aforementioned metal oxide nanocatalysts, thermogravimetric analysis (TGA) was employed. A set nanoparticle dispersion was mixed with a solution of human serum albumin (HSA) of known concentration. Protein-coated NPs were collected by centrifugation and subsequent washes removed surplus proteins (Figure S2, Supporting Information). Dried samples underwent TGA analysis, as illustrated in Figure 1f for CeO_2-NP with HSA. During the controlled heating/combustion process, initial water loss is evident (30–160 °C). A more significant weight reduction appears between 200–400 °C, coupled with an increase in the DSC-like signal. When compared to pristine nanoparticles, this second weight loss can be attributed to the organic corona's combustion, facilitating its quantification. Applying this protocol to each

nanomaterial revealed consistent quantifications, depicting the HSA protein corona (*w*%) in Figure 1g. Notably, HfO_2 displayed the most considerable protein corona weight fraction at over 32%, whereas the CeO_2–BG hybrid had the least at under 2%, a difference that may be partially attributed to the different particle sizes and shapes of these nanomaterials. Solely using individual protein solutions does not capture biological fluid complexity, thus the experiments were repeated with human serum. To assess variations in human serum, a conventional Bradford assay was employed to initially quantify the protein content in the respective biofluid. With human serum, the protein corona in the CeO_2–BG hybrid increased to 8%, and 33% in BG, but decreased to 23% in HfO_2, hinting at protein-specific interactions. Comparing the amount of adsorbed human serum proteins to the available surface area, evaluated by BET-analysis, it becomes apparent that the amount per area differs between the tested NPs up to an order of magnitude (0.8 mg m^{-2} for TiO_2 to 8.3 mg m^{-2} for Bioglass; Table S1, Supporting Information). In addition, we identified human serum protein aggregation on the nanocatalyst's surface via high-angle annular dark-field (HAADF) scanning transmission electron microscopy (STEM) coupled with energy dispersive X-ray spectroscopy (EDX) (Figures S3 and S4, Supporting Information). Such alterations due to the protein corona formation significantly impact the surface properties of the nanomaterials. For instance, Zeta-potential titration in Figure 1h revealed that while as-prepared nanomaterials have an isoelectric point at pH 2–3, those coated with human serum proteins shift toward pH 4–5 (Figure S5 and S6, Supporting Information). Additionally, the pH-dependent Zeta-potential of protein-coated NPs resembles the one of pure human serum. By modifying the surface charge, the nanoparticles' identity[25] shifts, directly affecting their colloidal stability and aggregate size, whereas NP was found to be predominantly stabilized through the protein coating (Figures S5–S7, Supporting Information). The adhering proteins form a dense network around the NPs, as observed by TEM (Figures S1, S3, and S4, Supporting Information). The adsorbed proteins were further characterized by SDS-PAGE, a prevalent method that permits protein separation and display. In the process, the protein corona was denatured and desorbed, and subsequently loaded onto an acrylamide gel. Proteins were sorted by molecular weight using electrophoresis and then stained using Coomassie blue (Figure 1i).

When compared with human serum (the original protein mixture), nanoparticles exhibit specific variances. Most notably, the protein profile of the NPs displays a diminished band ≈60 kDa, while, for instance, CeO_2, Mn_3O_4, HfO_2, and BG show a clear ≈15 kDa band, faintly perceptible in the serum. Similarly, the specific band ≈250 kDa is stronger post-desorption from the nanoparticles, as observed for CeO_2, Mn_3O_4, and HfO_2. The distinct bands post-adsorption and desorption suggest minimal protein degradation upon interaction with the metal oxide surface. Yet, no conclusions regarding the protein's intact structure or functionality can be drawn. In this initial data set, the nanoparticle-to-protein concentration ratio remained constant, pairing 1 mg mL^{-1} nanoparticle dispersion with 1 mg mL^{-1} proteins. However, varying protein levels in biofluids might influence the resultant protein corona. To evaluate this scenario, nanoparticles were first mixed with different human serum protein concentrations, spanning from excess nanoparticles (1:0.5) to surplus proteins (1:10) (Figure 1j). Four tested nanoparticles demonstrated a nearly consistent protein corona weight fraction across all conditions, indicating saturation with no additional protein accumulation, even under significant excess protein scenarios. Conversely, TiO_2 and the CeO_2–BG hybrid NPs displayed a distinct dependency. When more proteins were available during incubation, a more substantial protein corona was established. However, the provided quantification data do not elucidate whether a similar protein corona weight fraction alters the protein profile, or if a more extensive corona retains a consistent profile. Separating the protein corona from CeO_2, with varying initial protein treatments, suggests some alterations even when the overall quantity remains unchanged (Figure S8, Supporting Information). By using FT-IR spectroscopy, the nature of the nanocatalysts' surface chemistry was addressed, showing a high abundance of hydroxyl groups (Figure S9, Supporting Information). Presumably a major driving force for protein–NP binding can be therefore attributed to hydrogen bonding, whereas electrostatic forces and hydrophilic/hydrophobic forces are known factors to contribute likewise.[24,37]

Taken together, a robust TGA-based quantification protocol allowed us to investigate the interaction of metal oxide nanocatalysts with protein-containing body fluids. This straightforward technique ensured the complete combustion and therefore detection of the protein corona, not relying on a potentially incomplete desorption prior analysis. Even if various other protein corona quantification techniques are known,[38] the established protocol works highly reproducibly only requiring small amounts (a few mg) of sample material, enabling the investigation of and comparison between protein coronas formed on metal oxide NPs. As known exemplarily for nanoceria, the amount of adsorbed proteins depends on the surface charge, whereas absolute values might vary between the synthesis methods of the nanomaterials and the studied proteins.[39] The experiments showed that interestingly even under a large excess of proteins during the incubation period, the amount of adsorbed proteins stayed constant for four of the tested NPs. Most likely, the rapidly developed protein corona undergoes the Vroman effect,[40] whereas the first, non-specifically bound proteins are replaced by ones with a higher affinity to the nanocatalyst surface, however here without impacting the overall amount. The observed differences in the protein corona mass fraction seem not to depend on the accessible surface area, whereas in general topography and roughness besides crystallinity and functional surface groups of the NPs are known factors governing corona formation.[41]

2.2. Characterization of Protein Corona Composition via Proteomics

The influence of the protein corona is largely dictated by its specific protein composition. This composition is crucial as it directs the cellular association of nanoparticles and can even trigger potential immune responses.[42] Experiments illustrated in Figure 1i revealed a discernible pattern of adsorbed human serum proteins on the nanocatalyst surfaces. However, detailed characterization necessitates proteomics analysis. Initially, proteins adsorbed on the metal oxides were desorbed and subsequently enzymatically digested (details workflow can be found

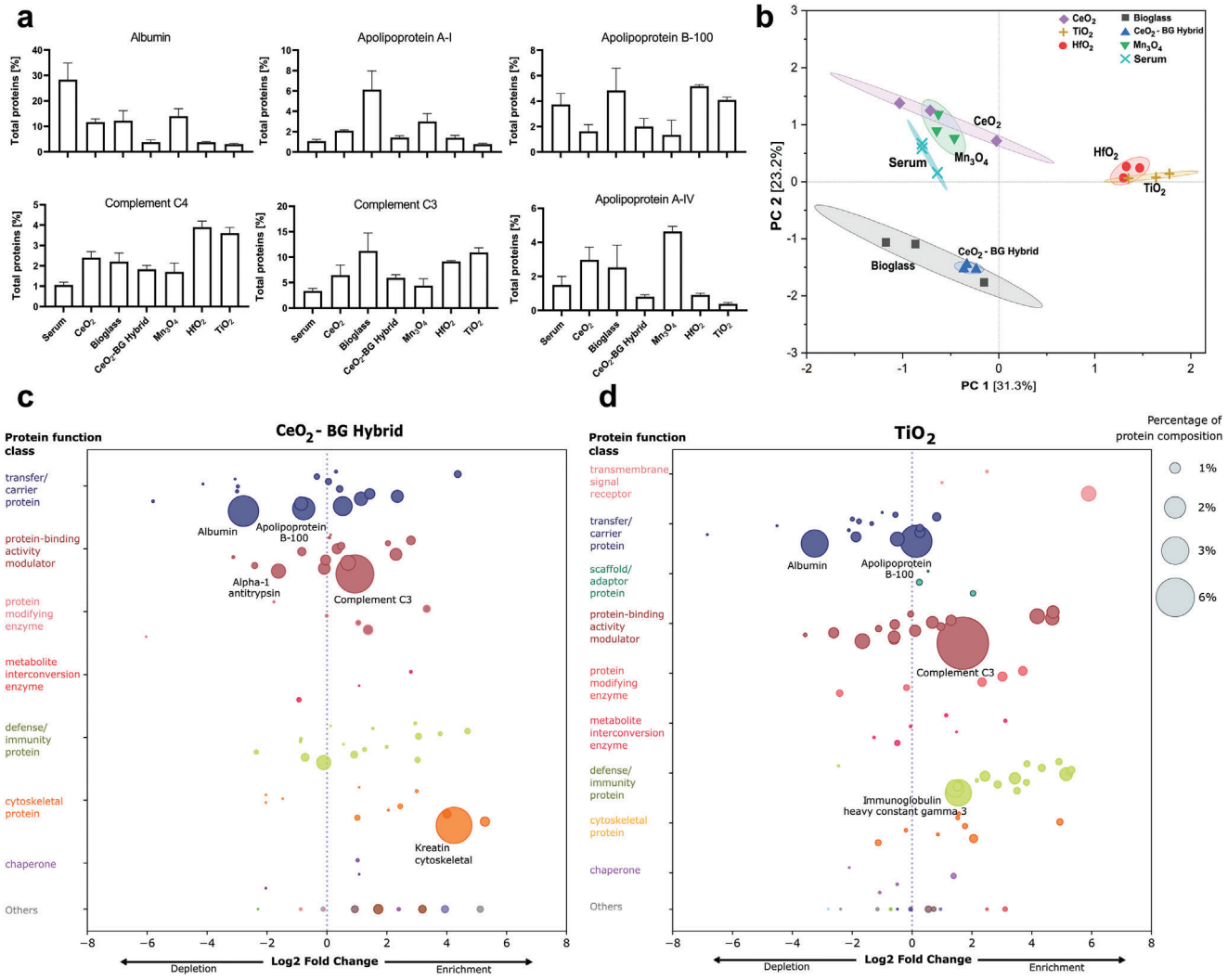

Figure 2. Proteomic profile of surface adsorbed proteins. a) Relative abundance of the six most common proteins found in human serum-coated nanoparticles (mean ± SD, $n = 3$). b) Comparison of the protein profile for the 100 most abundant proteins by principal component analysis (PCA) (ecliptic confidence interval 2σ, $n = 3$). c) Proteomics analysis of absorbed proteins shown as enrichment/depletion map compared to the protein profile found in human serum for CeO_2–Bioglass hybrid and d) TiO_2 nanoparticles. Circle size represents the relative abundance of the proteins found on the NP surface. Categorization of the main protein function by Panther classification (mean, $n = 3$).

in the Supporting Information). These protein fragments were subjected to a liquid chromatography-high-resolution mass spectrometry (LC–MS) analysis, facilitating the distinct separation and identification of the peptides. The acquired data, when matched with a database for *Homo sapiens* (Swissprot), enabled the reconstitution of the corresponding proteins. This semi-quantitative method not only delineates the exact protein corona but also facilitates comparison with the primary composition in human serum, shedding light on affinity-driven profile alterations. **Figure** 2a consolidates the relative abundances of the six most predominant of the ≈280 identified proteins in human serum and on coated metal oxides. Notably, the albumin concentration drops markedly from ≈30% in serum to 14% on Mn_3O_4 and as low as 3% on TiO_2 nanoparticle surfaces. In contrast, other abundant proteins, such as complement factors (C3 and C4) and apolipoproteins (A-I, A-IV, and B-100), display varied trends of enrichment and depletion. To understand the discerned protein patterns, an unsupervised multivariate statistical analysis encompassing the 100 most prevalent proteins was executed. Figure 2b showcases the results of this principal component analysis (PCA), with close clustering indicative of analogous protein profiles. Consequently, the profiles of TiO_2 and HfO_2 nanoparticles appear markedly similar, as do those of CeO_2 and Mn_3O_4. Interestingly, the protein profile of the CeO_2–BG hybrid aligns more closely with BG than with CeO_2 alone. A comprehensive analysis of the protein corona entails understanding not just the proteins but their inherent functions. Proteomic findings are depicted as enrichment/depletion maps relative to the protein profile observed in human serum (Figure 2c,d). Here, proteins are categorized based on the Panther classification system by their primary biological function.[43,44] The circle dimensions signify the relative abundance in the identified protein

corona. Enrichment profiles for CeO_2–BG hybrid and TiO_2 are presented as examples, while comprehensive profiles are accessible in Figures S10–S15 (Supporting Information). Interestingly, cytoskeletal proteins like Keratins (type I and II) were highly enriched from 0.3% in serum to 3.5% on BG and 8.2% on CeO_2–BG hybrid NPs, in contrast to all other tested NPs (Figure 2c,d). Notably, some of the significantly enriched proteins, beyond complement factors, belong to the defense and immunity class, as well as to the protein-binding activity modulators.

These analytical outcomes suggest a distinct interaction between each nanomaterial and the protein solution, resulting in a unique corona profile. Employing bioinformatic tools can elucidate the underlying mechanisms of this affinity-driven adsorption. An attempt was made to correlate protein sizes with the enrichment/depletion patterns, but no size-dependent influencing factor emerged (Figures S10–S15, Supporting Information). Additionally, the net charge of each protein was determined by summing the individual charges of its constituent amino acids. A discernible trend was observed: positively charged proteins showed enrichment on the negatively charged metal oxide surface. Not unexpectedly, this trend was absent for proteins bearing a negative net charge (Figures S10–S15, Supporting Information).

The outlined analysis sheds light on the biological identity of the metal oxide nanoparticles when encountering a biological fluid, such as plasma or blood. We observed significant differences between the profile of adsorbed proteins, whereas all NPs had the depletion of albumin and the enrichment in certain complement factors in common. This implies affinity-driven surface interactions between physio-chemically rather similar metal oxide particles and protein-rich bio-fluids, although no clear correlation to NP characteristics like specific surface area was found. During this process, we cannot exclude that proteins get entrapped non-specifically between nanoparticles, as described for the interparticle space of aggregated, spherical polystyrene NPs.[45] However, as protein adsorption on metal oxides did not lead to more pronounced aggregation, the proteomics results are expected to be minimally affected by this effect. We further linked the protein's nature to its main biological function and found the class of defense/immunity proteins predominantly enriched on all NPs. This could be interpreted as the first step of an immune response, whereas proteins automatically label foreign particles for immune cell recognition. However, it is important to note that this main-function assignment comes with the limitation that several classifications are possible, and even within the Panther classification, multiple functions are described. The bioinformatics classification and analysis revealed moreover a depletion of lipoproteins and proteins involved in coagulation, as well as an enrichment in various compartments of the complement pathway. This indicates that immunoglobulin and acute phase response proteins showed an increased affinity for the investigated nanocatalysts. The outlined tools could be used in future research to even predict the protein adsorption on nanocatalysts by statistical models and supervised learning.[46] However, since protein adsorption on the negatively charged nanoparticles did not correlate with protein size and only showed a weak correlation with charge, it suggests that electrostatic effects are only a minor factor in the protein-particle interaction, in line with previous reports on other silica-based nanoparticles.[26]

2.3. Seroma Model: Nanomaterial Corona Characteristics

After elucidating the fundamental mechanisms of protein corona formation on metal oxide nanoparticles, we investigated the impact of NP-protein interactions in (pre)clinically relevant conditions. The CeO_2–BG hybrid, encompassing diverse functionalities, has been identified as a potent therapeutic agent for treating wound-associated seromas. For an examination akin to clinical conditions, seroma fluid (SL) samples were sourced from patients and combined (n = 4). The protein corona resulting from this blend constituted ≈24% of the weight of the coated CeO_2–BG hybrid nanoparticles (**Figure** 3a), a proportion analogous to coronas formed from human serum with heightened protein concentrations. Subsequent proteomics investigations delineated the predominant proteins present in the seroma fluid and those adsorbed onto the NP surface (Figure 3b). Notably, albumin levels saw a significant reduction, decreasing from roughly 23% in seroma fluid to a mere 0.8% in the NPs. Among the dominant proteins on the NPs, several are recognized as agents of opsonization—i.e., the accumulation of (complement) proteins on the NP surface, signaling them for immune cell-mediated removal. To further discern the characteristics of the formed corona, the identified proteins were categorized based on their functional classes and then matched to their respective enrichment/depletion profiles (Figure 3c; Figure S16, Supporting Information). As per the Panther classification system, the predominant proteins belong to categories such as protein-modifying enzymes, intracellular signaling molecules, and extracellular matrix proteins. After having studied the native protein coronas that form around the investigated NPs, we explored strategies to deliberately influence corona formation. This was achieved by modifying the surface of CeO_2–BG hybrid NPs through covalent methods like PEGylation and meso-2,3-dimercaptosuccinic acid (DMSA) coating (Figure S17, Supporting Information). Surface treatment with a synthesized 1 kDa PEG-silane resulted in an undetectable protein corona, whereas DMSA substantially augmented the protein corona formation from 13% (pristine/as-prepared nanoparticles) to 21% (Figure 3d). The influence of these treated NPs on macrophages—the primary immune cells known for foreign material (NP) internalization—was assessed. Viability outcomes (Figure 3e) showed discernible disparities between the various protein–corona variants and the as-prepared nanoparticles.

Additionally, particle uptake dynamics were probed using ICP–MS (Figure 3f). Given that Ce levels in macrophages correspond to phagocytized nanoparticles, it was observed that CeO_2–BG hybrids with adsorbed proteins were more readily internalized compared to their uncoated counterparts. Conversely, PEGylated particles maintained a consistent uptake rate. Interestingly, the DMSA-coated particles showcased an uptake rate that was nearly triple, irrespective of human serum protein adsorption. Such differences could be explained due to changes in the surface properties such as Zeta-potential, even if the different CeO_2–BG nanoconjugates showed similar particle sizes. In contrast to the PEGylated surface modification (11% *w*/*w*), the DMSA-coating resulted in sparse organic coating (2% *w*/*w*) possessing a significant amount of free hydroxyl groups, as well as carboxyl and thiol groups in theory, likely the driving force for augmented protein interaction and

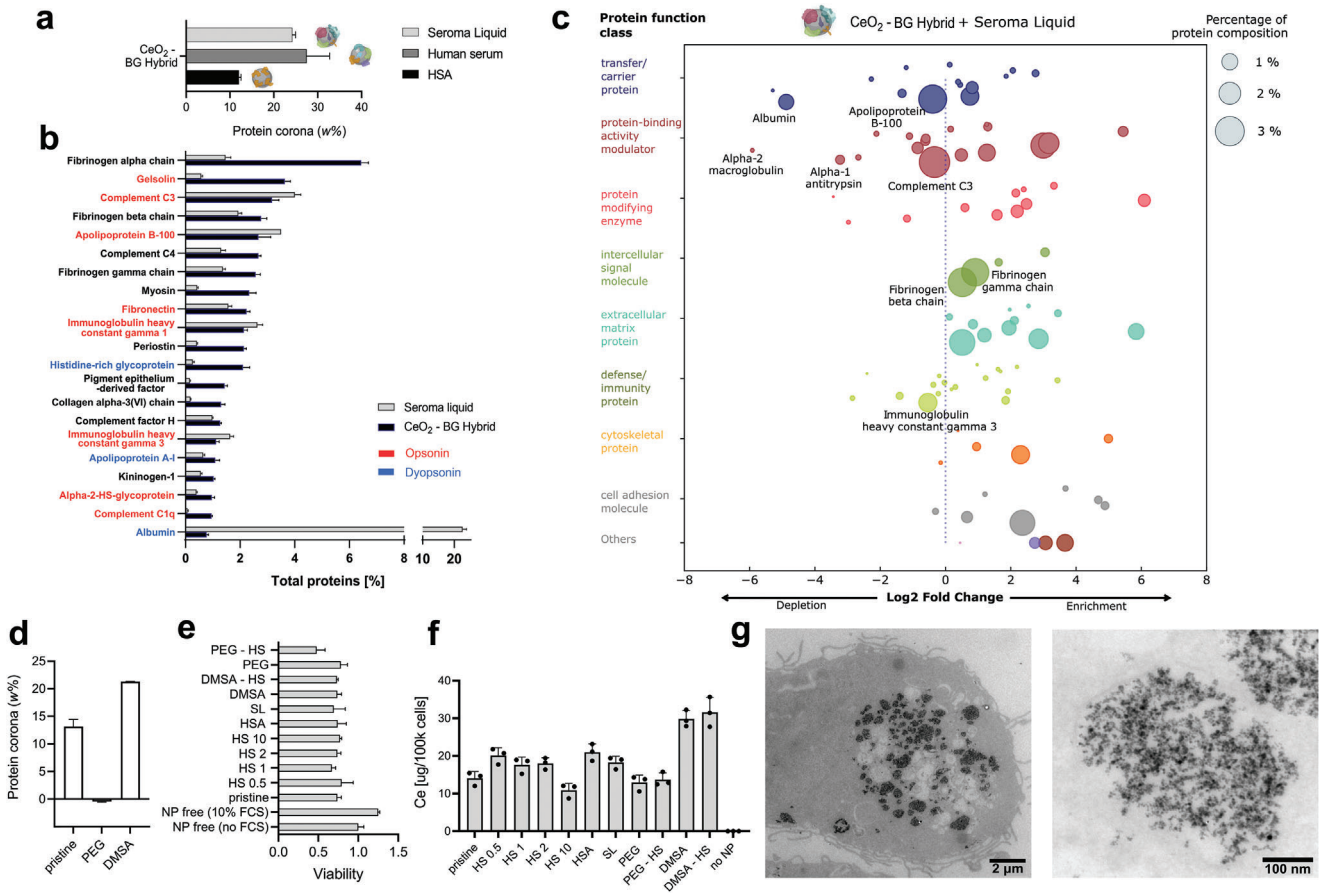

Figure 3. Immune cell activator enrichment on CeO_2–Bioglass hybrid nanoparticles for seroma treatment. a) Amounts of protein corona formed by different biofluids (incubation ratio 1:10 NP: proteins; mean ± SD, $n = 3$). b) Relative abundance of the 21 most common proteins found in aspirated human seroma liquid compared to the protein fraction which aggregates on CeO_2–Bioglass hybrid NP (mean ± SD, $n = 3$). Red-colored proteins indicate opsonins, blue dyopsonins. c) Proteomics analysis of absorbed proteins shown as enrichment/depletion map compared to the protein profile found in human seroma liquid for CeO_2–Bioglass hybrid nanoparticles. Circle size represents the relative abundance of the proteins found on the NP surface. Categorization of the main protein function by Panther classification. (mean, $n = 3$). d) Surface modification of CeO_2–BG hybrid NP by PEG and DMSA alters the amount of absorbed proteins from human serum (mean ± SD, $n = 3$). e) Macrophage cell viability after 1d incubation of 50 µg mL^{-1} nanoparticle solution (mean ± SD, $n = 3$). f) Nanoparticle cell uptake evaluated as Ce concentration per 100k cells after 1d of incubation. g) TEM image of a macrophage that internalized CeO_2–BG hybrid NPs coated with human serum proteins (left). The magnified region with phagocytosed NPs (right).

cellular uptake (Figure S17, Supporting Information). To verify the internalization and uptake of the NP, macrophages were treated with as-synthesized, human serum protein-coated and human seroma liquid protein-coated CeO_2–BG Hybrid NPs, fixed, stained, dehydrated, epoxy-embedded, ultrathin sectioned, and imaged with TEM (Figure 3g, Figure S18, Supporting Information). For all investigated conditions, the particles (with and without protein corona) were located in vesicular compartments, exhibiting the characteristics of endo-/lysosomes. Morphology-wise there was no significant difference identified for as-produced and protein corona-coated NPs within the cellular compartments.

2.4. Seroma Model: Nanomaterial In Vivo Biodistribution

After confirming cytocompatibility and uptake into macrophages, samples from CeO_2–BG hybrid NPs applied in a seroma model[35,47] in rats were investigated. Histological sections were stained with CD68 to discern macrophages. Concurrently, for direct NP visualization, the same sections underwent preparation for scanning electron microscopy (SEM) and EDX mapping (**Figure** 4a,b). Correlative analysis revealed a robust positive relationship between CD68-positive cells (macrophages) and nanoparticle distribution. ≈98% of the observed macrophages in granuloma and 35% of the free macrophages were found to co-localize with nanoparticles (Figure 4c). On the other hand, no NPs were found outside of macrophages. Additionally, there were no significant nanoparticle clusters detected within the connective tissue, which led us to the conclusion that >99% of nanoparticles are found in tissue-resident macrophages. Collectively, these observations corroborated the strong association between nanoparticles and macrophages in vivo, in line also with the protein corona composition (Figure 3b,c). Since the bioactivity of the mixed metal oxide NPs is mainly based on the redox activity of Ce, we

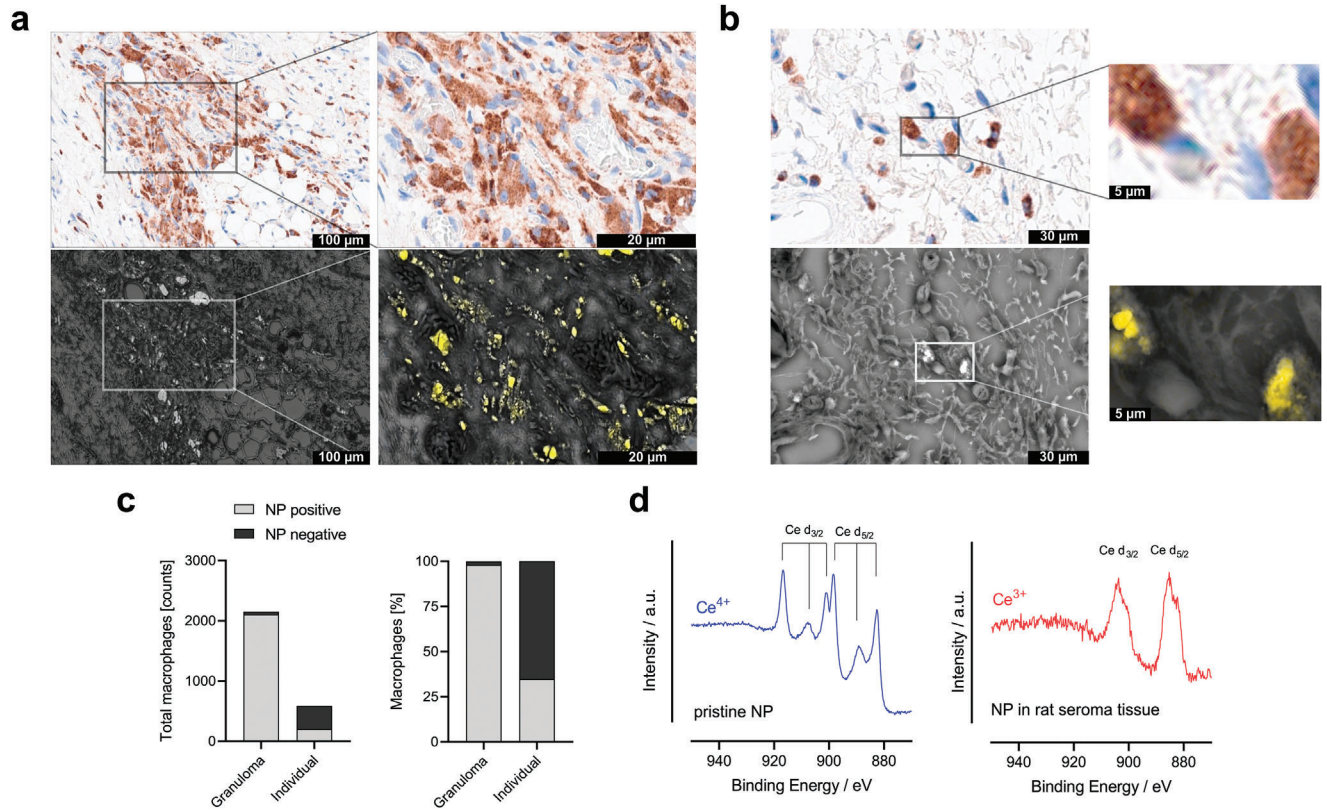

Figure 4. CeO_2–Bioglass hybrid nanoparticles for in vivo seroma treatment. a) Histological rat tissue sections after seroma treatment with CeO_2–BG hybrid NP. Blue staining (hematoxylin counterstain) indicates cell nuclei, and brown staining (CD68 immunohistochemistry) macrophages (upper panel). Correlation with SEM images (lower panel) of the corresponding regions shows electron-dense areas, while the magnification with elemental mapping via EDX identifies cerium (yellow). b) Histology-SEM correlation down to a single cell level, as macrophages internalize the CeO_2–BG hybrid NPs. Macrophage staining (brown, upper panel) and cerium elemental mapping (yellow, lower panel) co-localize. c) Evaluation of the macrophages associated with NPs. Shown as a total number of counted cells (left) and a fraction of the cell population (right) within the granuloma or as individual macrophages. No nanoparticles were found outside of macrophages. d) XPS spectra of Ce. The blue spectrum of as-synthesized CeO_2–BG hybrid NP shows features dominantly related to the Ce^{4+} state, whereas in situ measurements of NP within the rat seroma tissue after 42 days show features dominantly related to Ce^{3+} (red spectrum).

examined if the initial redox state might have altered after tissue injection and macrophage uptake. As shown in Figure 4d, the redox state of the pristine CeO_2–BG hybrid NP is predominantly Ce^{4+}, whereas in situ X-ray photoelectron spectroscopy (XPS) measurements of the tissue sections revealed a complete shift to Ce^{3+}, given that the XPS spectra of Ce redox states are in accordance with previous studies.[48]

This points toward a more complex scenario than a simple consumption of the NP's enzyme-mimicking capacity. Typically, Ce^{3+} is oxidized to Ce^{4+} during H_2O_2 decomposition, followed by back-cycling.[49] However, the impact of both states regarding the enzyme-mimicking activity is discussed controversially.[32,50,51] Our findings could be therefore interpreted as a biotransformation-induced phenomenon, due to the formation of catalytically inactive cerium phosphate with the oxidation state Ce^{3+}.[22] This indicates that successful ROS reduction during wound healing inflammation[8] management happens faster than biotransformation and catalytic inhibition. The outlined experiments thus aim to bring us a step closer to understanding the complex interplay between redox state and catalytic potential[32,49] within a biological environment.

Analyzing the formed seroma protein corona showed that HSA as a prominent dyopsonin is highly reduced, likely through the Vroman effect, whereas highly abundant proteins that initially adsorb to the surface are replaced by ones with a higher affinity.[40] This observation is accompanied by the accumulation of different opsonins, as outlined in Figure 3b and Table S2 (Supporting Information), generally marking the nanocatalysts for immune cell uptake. Additionally, proteins involved in blood coagulation and cell adhesion like fibrinogen and fibronectin found to be strongly enhanced on the CeO_2–BG hybrids, supporting their impact on wound healing and seroma closure.[35] However, comparing the macrophage uptake of different protein-coated nanoparticles comes with an inherent limitation, since the culture medium itself contains proteins as a nutrient source for the macrophages. We aimed to reduce this influence by conducting experiments in the FCS-devoid medium, however, a certain protein amount in the culture medium is inevitable. This resulted most likely in a protein coating of the native NPs[52] and potentially even in a co-adsorption of the protein-coated ones, however, with the outcome of increased uptake when coated prior with human body fluid proteins. Interestingly, HSA (dyopsonin)

and seroma liquid (predominantly opsonin)-coated NPs showed a similar uptake into macrophages, indicating that culture-medium derived markers likely change the soft protein corona, defined as the layer of proteins interacting with the directly physisorbed ones on the NPs (hard corona). On the other hand, PEGylation of NPs is known to induce a stealth effect, as well as to foster selective protein absorption,[53] which is in agreement with our results, showing prevention of protein adsorption and no enhanced uptake. Such encapsulation can generally shield the NPs from aggregation, opsonization, and phagocytosis, leading to extended circulation time within the host tissue and potentially delayed macrophage clearance.[54,55] These improvements may influence the antioxidant and anti-inflammatory effect and reduce the macrophage-based granuloma formation. Interestingly, the opposite was observed for the DMSA coating, whereas the enhanced protein adsorption could result from the formation of covalent disulfide bridges between the DMSA-NPs and the free proteins. Protein-NP charge and hydrophobicity are reportedly an important factor for macrophage uptake,[56] hence supporting our observations. In summary, we showed that these cellular tests can serve as a valid tool to study the influence of nanocatalyst surface modification on macrophage uptake. However, certain limitations outline the need for more elaborate tests, depicting a complex in vivo scenario, in order to understand NP fate.[57] This aspect was complemented by the presented analysis of the CeO_2–BG hybrid NPs deployed for seroma treatment in a rat model (Figure 4). The observed co-localization suggests a sufficient opsonization of the NPs and subsequent efficient internalization by macrophages, overall preventing the NPs from escaping the application side. The given insights have the potential to pave the way for tailored NP applications in wound healing and seroma treatment, tuning or evading the macrophage uptake, ultimately governing the inflammatory response. The presented methodology of in situ electron microscopic analysis (SEM, XPS) in correlation with histological and immunohistochemistry investigations can be applied in the future to investigate NP interaction with other immune cells, such as neutrophils.

2.5. Protein Corona Influences Catalytic Activity

After characterizing the protein corona composition and its influence on the in vitro and in vivo fate of the NPs, the influence of the protein corona on the catalytic activity of these metal oxides was investigated. The first group of catalytically active nanoparticles (CeO_2, Mn_3O_4, the CeO_2–BG hybrid) demonstrates an ability to scavenge reactive oxygen species (ROS), facilitated by surface-mediated redox cycling. Specifically, this group exhibits catalase (CAT) mimetic activity, reducing H_2O_2 to H_2O and O_2, and superoxide dismutase (SOD) mimetic activity, which converts superoxide anion ($O_2^{\cdot-}$) into H_2O_2 (**Figure 5a**). We first determined the CAT activity of CeO_2, Mn_3O_4, the CeO_2–BG hybrid, and BG by itself. This assay leverages the inherent UV absorption of H_2O_2 at 240 nm, executed in a multi-well plate format, which facilitates concurrent testing under various parameters. A consistent linear detection regime was confirmed throughout the experiment (Figure 5b). For subsequent nanoparticle evaluations, the probes aligned with those used in earlier protein corona ratio tests (refer to Figure 1j). Figure 5c presents the H_2O_2 concentrations remaining from in initial 50 mM solution post 2, 6, and 24 h of interaction with the metal oxide nanoparticles relative to their initial protein-incubation ratios or as pristine particles without a protein corona. The CAT mimicry efficacy of the nanoparticle dispersion is inversely proportional to the detected H_2O_2 post-nanoparticle interaction. As anticipated, BG nanoparticles, on their own, did not exhibit significant CAT activity, while both Mn_3O_4 and CeO_2 showed considerably reduced H_2O_2 concentrations within the 2–24 h window, especially in the absence of a protein corona (Figure S19, Supporting Information). Conversely, protein-coated CeO_2–BG hybrid samples exhibited augmented activity compared to the pristine nanoparticles, correlated with increased colloidal stability. These findings naturally led to the question of whether protein-coating-induced shifts in nanozyme activity could be reversed via protease degradation. As depicted in Figure 5d, proteolytic digestion of the protein corona on human serum protein-coated Mn_3O_4 and CeO_2 partially restored CAT activity, as evidenced by decreased H_2O_2 levels. SOD activity generally indicated diminished activity for nanoparticles with a protein coating (Figure 5e). In additional experiments, the effect of the protein corona on radical generation was investigated. Metal oxide NPs were irradiated by UV light or X-rays to assess ROS production potential. This photocatalytic cleavage can yield hydroxyl-radicals (·OH) from H_2O or superoxide anions ($O_2^{\cdot-}$) from molecular oxygen (O_2), as depicted in Figure 5f. A widely accepted fluorescence probe (DCF) was utilized to detect these radicals, confirming potent ROS production in the case of TiO_2 nanoparticles. A decline in photocatalytic ROS production was observed for protein-coated samples, but protease treatment partially restored this ability (Figure 5g). HfO_2 nanoparticles, while non-reactive under UV (>300 nm) illumination, responded under X-ray exposure. This mechanism is being considered to amplify the efficacy of X-ray doses in cancer radiotherapy. As Figure 5h demonstrates, protein-coating of nanocatalysts significantly diminishes the dose enhancement factor (DEF). This attenuation is even more pronounced for TiO_2 nanoparticles. However, again, protease exposure can restore their ROS-generating capabilities under X-ray exposure (Figure 5h, right panel). To address the question of how fast such protein corona formation affects the catalytic NP properties, a series of time-resolved electron paramagnetic resonance (EPR) spectroscopy measurements were conducted. As shown in Figure 5i, TiO_2 NP produced ROS after UV irradiation, which formed with the radical scavenger DMPO a conjugate with the typical features of DMPO-OH radicals. In situ, the addition of HSA to the NP dispersion leads to a drastic reduction of the detected signal within 2 min. Such a fast quenching process was further confirmed when adding the protein solution directly at the start of the experiment (Figure 5j).

However, within the time course of the experiment (30 min), the detected ROS levels from the TiO_2-HSA dispersion recovered, though to a lower level compared to the control.

The outlined data show in a holistic approach how nanozyme activity is impaired within minutes by protein adsorption and restored after proteolytic degradation of the formed corona. The reduced nanocatalysts performance could be the result of decelerated diffusion of the ROS toward and from the NP surface, of partially (irreversible) binding of catalytic sites, or due to attenuated charge transfer processes within the NP surface. However, no quantification of the remaining protein

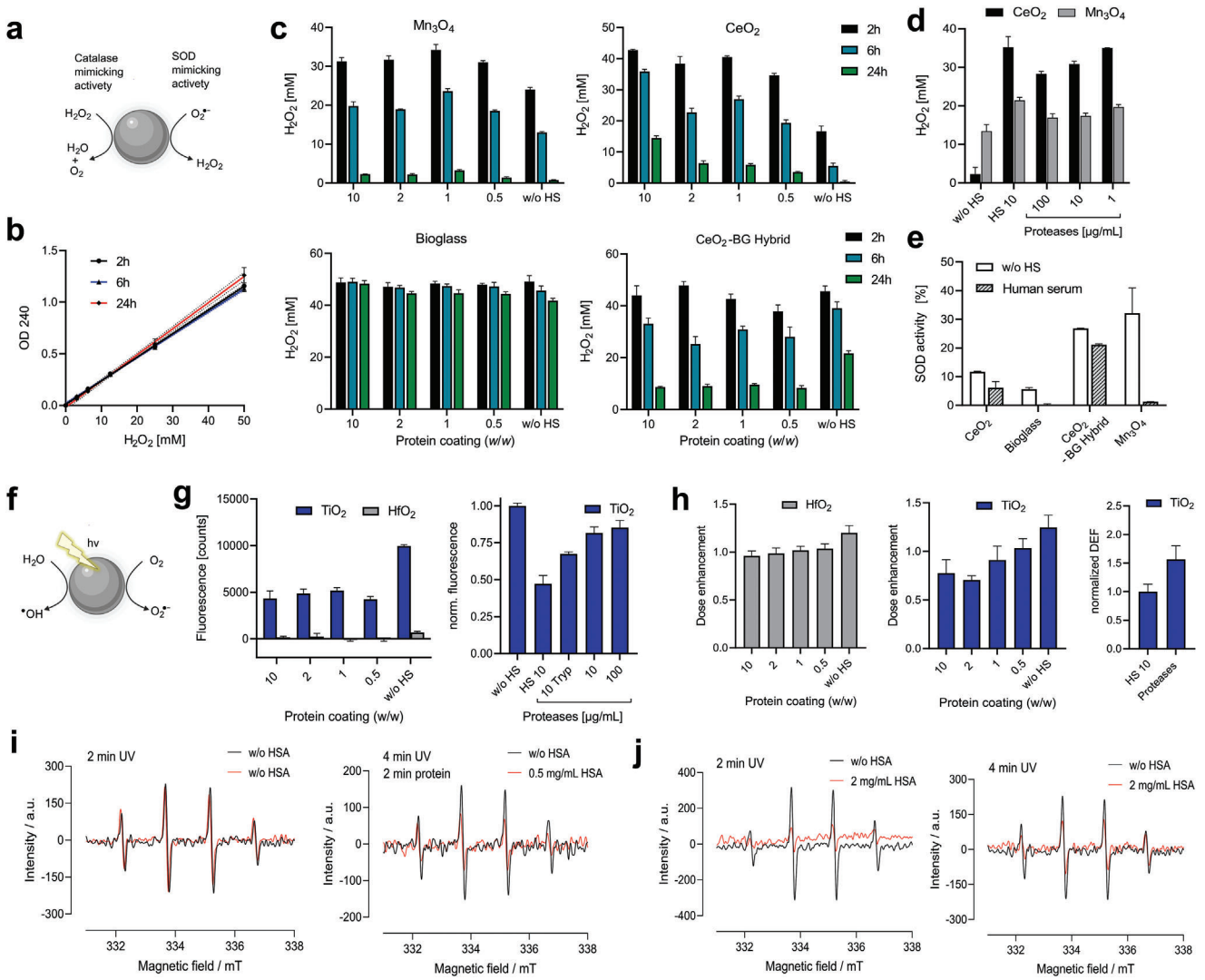

Figure 5. Effect of surface-absorbed proteins on catalytic activity. a) Illustration of metal–oxide NPs exhibiting ROS scavenging (CAT-catalase, SOD-superoxide dismutase) properties. b) Linear calibration curves of the H_2O_2 quantification assay remain stable over the time course of the experiment (mean ± SD, $n = 3$). c) H_2O_2-scavenging activity of different NP after incubation with different protein ratios from human serum (HS) (initial H_2O_2 concentration = 50 mM, mean ± SD, $n = 3$). d) Addition of proteases restore partly the reduced H_2O_2-scavenging ability of CeO_2 and Mn_3O_4 NPs after protein absorption (mean ± SD, $n = 3$). e) SOD-activity of pristine and human serum coated NP (mean ± SD, $n = 3$). f) Illustration of metal–oxide NP generating ROS under irradiation. g) Left plot: Photocatalytic effect of NP produces ROS after UV illumination, as measured by DCF. Right plot: Protease addition partly reverses the loss in activity (Tryp-Trypsin protease, mean ± SD, $n = 3$). h) DCF assessed ROS production for TiO_2 and HfO_2 after 12 Gy X-ray irradiation, expressed as dose enhancement factor and partly restored activity after protease treatment (mean ± SD, $n = 3$). i) Time-resolved EPR spectra of DMPO-OH-radicals generated by TiO_2 NP during UV irradiation. Two independent experiments result after 2 min of UV irradiation in a similar DMPO-radical signal (left) whereas the addition of 0.5 mg mL^{-1} HSA leads to a strong decrease (right). j) Photocatalytic ROS production is strongly hindered after initial protein addition (left) but slightly recovers within the time course of the experiment (right).

corona was performed after protease digestion. Most likely partwise removal of the adsorbed proteins could be the reason for improved activity of TiO_2 NP, but not to the same level as the non-coated NP possess. These results are in line with a recent study showing the recovery of gold nanoparticle activity through proteolysis.[31] Given that HfO_2 NPs are currently in clinical use to treat advanced soft tissue sarcoma via photon radiotherapy,[20] the implications of our study should be considered for future research. This holds especially true, since the pharma company Johnson & Johnson recently invested in a multi-million-dollar project aiming for the global license of NBTXR3 (HfO_2),[58] currently accessing its efficacy in treating head and neck cancer within a Phase 3 study.[59] As protein adsorption reduced the DEF after X-ray irradiation, strategies to minimize the absorption of biomolecules, such as proteins, on HfO_2 NPs could therefore enhance their in vivo activity. Thus, the simultaneous injection of proteases might possibly yield a positive effect as well.

The only notable exception to these trends is the CAT activity of the CeO_2–BG hybrid, which increased upon the formation of a protein corona, likely due to improved colloidal stability and

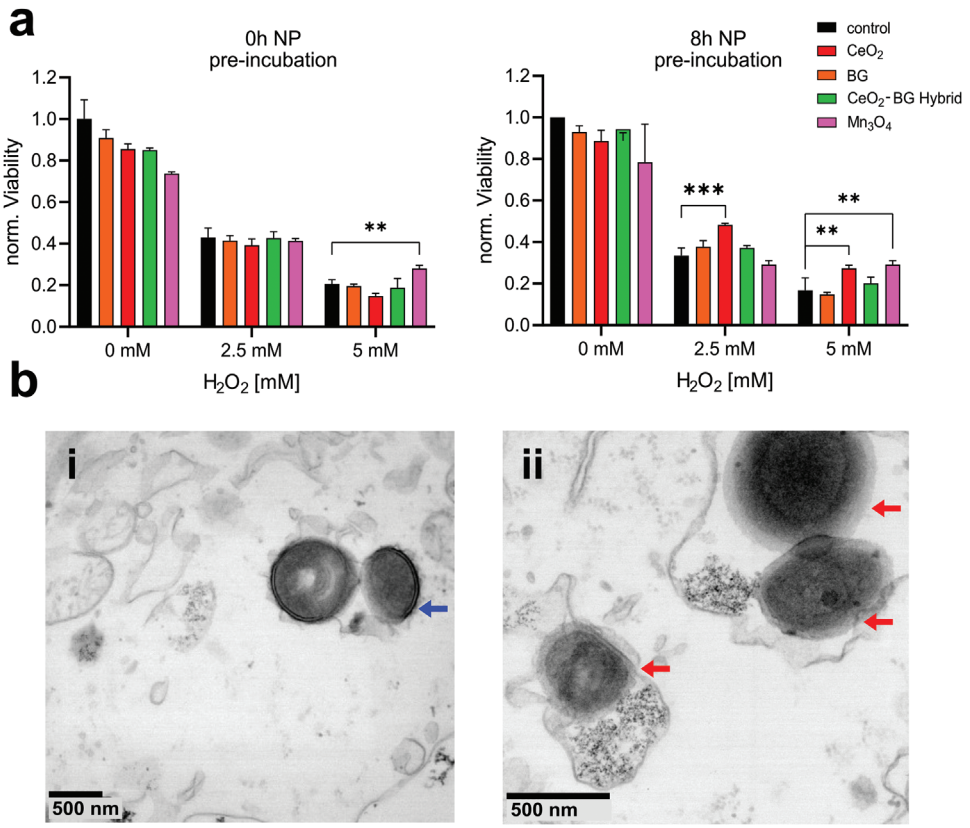

Figure 6. Functional activity assay in macrophages. a) Macrophage cell viability after 2 h incubation at varying H_2O_2 levels. Cells were pre-loaded (8 h NP pre-incubation) or not pre-loaded (0 h NP pre-incubation) at 100 µg mL^{-1} CeO_2, BG, CeO_2–BG or Mn_3O_4 (5 µg mL^{-1}) nanoparticles, reflecting internalized and non-internalized nanoparticle scenarios, respectively (mean ± SD, $n = 3$; one-way ANOVA, ns, $^{**}p = 0.002$, $^{***}p = 0.0002$). b) Antibacterial intracellular activity of CeO_2–BG hybrid NPs. TEM micrographs of *S. aureus* infecting monocyte-derived macrophages. (i) w/o NPs, intact cell membrane (blue arrow). (ii) NPs associated with cell membrane damage (red arrow).

the formation of a loosely associated protein corona not obstructing the active sites. Since protein adsorption was found to have a major impact, as seen in the scavenging experiments conducted from a single protein (HSA) solution, we did not investigate how the adsorption of various other biomolecules like DNA, small molecules or lipids would affect the nanozyme activity. Given the presented results, we cannot exclude a partial activity shift after incubation in complex biofluids like human serum or human seroma liquid due to the adsorption of other biomolecules besides proteins. Future research endeavors should focus on engineering surface chemistry by organic ligands in order to find the optimal balance between colloidal stability and catalytic activity for in vivo applications. General design strategies to enhance stability typically rely on the covalent or non-covalent attachment of surface ligands. However, such modification could potentially impair the surface-mediated catalytic activity. Hence, optimal NP design needs to balance between stability and activity, depending also on the specific application. Local administration of nanocatalysts (HfO_2 for cancer treatment or CeO_2–BG for wound management) might benefit from a spare surface modification hampering NP aggregation based on, e.g., carboxylate ligands.[60] Different strategies should be considered for intravenous application, including zwitterionic coatings, PEGylation, or polysaccharides, improving circulation half-time. Such approaches may not only improve colloidal stability but can also enhance the biocompatibility and targeting of the nanoparticles.[61]

2.6. Functional Activity Assays in Target Cells

To evaluate the efficacy of the nanoparticles in complex biological systems, functional activity assays were conducted using human macrophages, given that these cells are the primary target cells for the investigated NPs. This step is crucial as it determines if the nanoparticles can maintain their intended functions amidst the myriad of biological interactions and challenges present within such environments. The ability of nanoparticles to protect cells from oxidative stress was tested using hydrogen peroxide as an external trigger. Macrophages were stressed with H_2O_2 at two concentrations, 2.5 and 5 mM, which led to ≈40% and 20% cell viability after 2 h (**Figure 6** a, control). Four nanoparticles, namely CeO_2, BG, CeO_2–BG, and Mn_3O_4, were tested for their potential to protect cells from oxidative stress. Two scenarios were tested, one where only extracellular nanoparticles were present, and a second where cells with internalized nanoparticles were present before cells were stressed with H_2O_2. To induce those scenarios, nanoparticles were either administered 0 or 8 h to cells before H_2O_2 was added. At 100 µg mL^{-1}, the nanoparticles alone were

well tolerated (viabilities > 70%). Only in the case of Mn_3O_4 NPs and 8 h NP pre-incubation, 100 µg mL^{-1} led to high toxicity, so the concentration for this particular case was reduced to subtoxic 5 µg mL^{-1}. When nanoparticles were present only external to cells, cell viabilities with and without nanoparticles were very comparable to one another at both H_2O_2 concentrations, hinting to rather little ROS scavenging activity. Only the most catalytically active candidate, Mn_3O_4, provided a significantly enhanced cell viability compared to control cells at the higher 5 mM H_2O_2 concentration. When cells were pre-loaded with nanoparticles for 8 h, however, higher cell viabilities in the case of CeO_2 and Mn_3O_4 were detected at both H_2O_2 concentrations compared to control cells, providing significant cell protection from oxidative stress.

This is well in line with the high CAT activity of these two materials found in cell-free tests. In conclusion, pre-loading cells especially with CeO_2 nanoparticles, or in other words internalized CeO_2 nanoparticles, provided cell protection from oxidative stress, while the presence of 100 µg mL^{-1} extra-cellular nanoparticles did not. This strongly supports the hypothesis that the NPs regain catalytic activity after uptake into endo/lysosomes where the protein corona is cleaved by proteases. Similarly, intracellular CeO_2–BG NP activity is supported by transmission electron micrographs of *S. aureus* infecting monocyte-derived macrophages. CeO_2–BG NPs contained in endo-/lysosomes and co-localized with *S. aureus* disrupt the *S. aureus* membrane to a noticeable extent (Figure 6b ii), further supporting the intracellular activity of the NPs after proteolytic degradation of the protein corona.[62] This observation is in line with recent literature, reporting intracellular reactivation of gold-NP catalytic activity after protease-induced corona degradation, whereas protease inhibitors could stop this endosomal process.[31]

3. Conclusion

In the outlined study, we presented a holistic approach to synthesize and characterize metal oxide nanocatalysts for biomedical applications and analyze their interaction with protein-containing body fluids. Interestingly, a large variation of the protein corona mass fraction was found between the nanocatalysts, depending in addition to it also on the protein composition of the body fluid. By means of proteomic analysis, it was possible to identify a significant decrease in the main serum component HSA on the NP surface, as well as an enhanced aggregation of immune cell markers like complement factors. We reveal how mixed metal oxide nanocatalysts, namely CeO_2–Bioglass hybrid NPs used for wound healing and seroma treatment, are uptaken by immune cells at the application side with remarkably high specificity (>99% of detected nanoparticles found in macrophages, no NPs detected in connective tissue). Likely through the absorption of opsonins, NP is marked for macrophages and internalized into the phagosome. The general formation of a protein corona on the metal oxide nanocatalysts was found to decrease CAT and SOD enzyme mimicking activities of CeO_2 and Mn_3O_4 NP, as well as the photocatalytic activity of TiO_2 and HfO_2 to produce ROS after UV or X-Ray exposure. We further demonstrate how such protein–corona induced reduction of the nanocatalysts properties is restored by protease-based corona digestion. This digestion mimics the intracellular process within the phagosome and could explain the in vivo activity of the nanomaterials, even after encountering protein-containing fluids. These findings collectively emphasize the crucial importance of environment-dependent interactions between nanocatalysts and complex biological fluids, significantly affecting the fate and activity of nanomaterials. The agnostic methodological toolbox presented in this study establishes a foundation for further exploration of the catalytic activity of nanomaterials in complex biological systems. This has the potential to assist in the design of new therapeutic interventions, fostering nanocatalyst applications in cancer treatment or antimicrobial therapies.

4. Experimental Section

All materials, if not stated otherwise, were purchased from Sigma–Aldrich or VWR Chemicals.

Nanoparticle Synthesis by Flame–Spray-Pyrolysis: Metal oxide nanoparticles were produced by liquid-feed flame spray pyrolysis according to previously established protocols.[17,18,32] Typically, 5 mL min^{-1} 0.3 M precursor solution was pumped to a water-cooled spray nozzle and dispersed by 5 L min^{-1} O_2, ignited by a CH_4/O_2 (1.5:3.2 L min^{-1}) flame. Particles were collected on a glass fiber filter located 70 cm above the flame and sieved through a 200 µm mesh.

Microwave Digestion and Elemental Analysis: Nanoparticles or NP-containing cells were digested in a high-pressure microwave (TurboWAVE, MLS GmbH, Germany) using polytetrafluoroethylene containers. 1–2 mg NP or 100 000 cells in medium were mixed with 3 mL of 65% HNO_3 p.a. (Merck) and 1 mL of 30% H_2O_2 p.a. (Merck) and digested at 250 °C, 120 bar for 18 min. Elemental composition was evaluated by analyzing the digested NPs via ICP-OES (Agilent, Santa Clara, CA).[7,63] Cerium levels were quantified using an ICP-MS (Model 7900, Agilent, Santa Clara, CA) by measuring isotope ^{140}Ce. ^{175}Lu served as an internal standard to correct for non-spectral interferences.[35,64]

Electron Microscopy: For TEM analysis, the as-produced and human serum protein-coated nanoparticles were drop-casted onto copper grids (EMR, Holey Carbon Film 300 Mesh), air-dried, and imaged with a Zeiss EM 900 microscope (Carl Zeiss Microscopy GmbH, Germany) at 80 kV and different magnifications. The particle size distributions were determined using ImageJ (1.54b). These grids were also analyzed with high-angle annular dark-field (HAADF) scanning transmission electron microscopy (STEM) coupled with energy dispersive X-ray spectroscopy (EDX) using a Talos F200X TEM microscope (FEI, 4 detector configuration, Super-X EDS) at 200 kV. A detailed protocol for the macrophage TEM micrograph preparation can be found in the Supporting Information. SEM-EDX analysis of histological rat tissue sections was performed with an Axia Chemisem (Thermo Fisher, NL). To this end, the cover slips from the histological sections along with the paraffin were removed by incubation in Xylene for 3 days. Samples were then air-dried and coated with 10 nm carbon (Leica EM ACE600) prior to analysis. In situ XPS analysis was performed with the same histological rat tissue sections, using a Nexsa G2 (Thermo Scientific) with 150 µm X-ray spot size.

Nanoparticle Characterization: X-ray diffraction analysis (XRD) was performed with a Bruker D2 2nd Gen Phaser (30 kV, 10 mA, SSD160 detector, Cu tube 1.54184 [Å] Kα radiation at 2θ = 10°–80° with a step size of 0.01°). Phase composition and crystallite sizes were determined using the Diffrac Eva (V3.1) software, after performing Rietveld parameter refinement. The surface area was determined based on the Brunauer–Emmett–Teller (BET) method at 77 K (Micromeritics, Tristar II Plus) as described previously.[65] Hydrodynamic size measurements (dynamic light scattering, DLS) and zeta-potential determination were performed with a Zetasizer Nano-ZS (Malvern Instruments), combined with an auto-titration unit (MPT-2) to access the isoelectric point. Fourier transform infrared spectroscopy (FT-IR) was performed on a Bruker Vertex 70 with an MCT detector (D313) and a Mikro-ATR "Golden Gate", Mark II accessory.

Nanoparticle Dispersion and Surface Modification: Typically, 20 mg NP were dispersed in water (1 mg mL^{-1} concentration, 10 min 90% ampli-

tude, Sonics Vibra cell VCX 500, cup horn) and incubated for 1 h at 37 °C with protein solution, matching a final ratio as indicated (e.g., ratio of 1:1 indicated 1 mg mL^{-1} NP with 1 mg mL^{-1} proteins). Protein concentration was pre-determined by the standard Bradford test, using a 96-well microarray (HIDEX absorbance plate reader). NP-protein solution was centrifuged for 20 min at 7800×g and washed twice with ddH_2O to remove access proteins and redispersed in 5 mL H_2O before determining concertation by drying and weighting an aliquot. Surface grafting of CeO_2–BG hybrid NPs by silane-PEG and DMSA was realized by modifying previously reported protocols.[66,67] A detailed description can be found in the Supporting Information.

Protein Corona quantification by Thermogravimetric analysis: About 5 mg of (Protein)-NP was inserted into a METTLER TOLEDO TGA/DSC 3+ and analyzed with the following temperature profile: 10min@40 °C; 10 K min^{-1} ramp to 140 °C; 10min@140 °C; 16.5 K min^{-1} ramp to 800 °C; 40 mL min^{-1} airflow. Weight loss was quantified from 160 °C (after the loss of physiosorbed water) and 700 °C (complete combustion of organic matter). The differences between pristine and protein-coated NP were determined and expressed as the amount of surface absorbed proteins, calculated with the following formulas:

$$\frac{\frac{mNP_{160°C}}{mNP_{40°C}}}{\frac{mNP_{700°C}}{mNP_{40°C}}} = w_{NP} \quad (1)$$

$$100\left((1 - w_{NP}) - \left(1 - w_{pristineNP}\right)\right) = \text{Protein corona (w\%)} \quad (2)$$

with $mNP_{160°C}$ ~ mass measured by TGA at T = 160 °C; w_{NP} ~ weight loss NP with proteins; $w_{pristine\ NP}$ ~ weight loss of pristine NP (dispersed and treated similar to NP without addition of proteins).

Proteomics Analysis: Proteomics analysis was carried out by the Functional Genomics Center Zurich (FGCZ). A detailed protocol can be found in the Supporting Information. In short, 2 µL of the protein solution or the NP-protein pellet was lysed in 4% SDS lysis buffer, reduced and alkylated with TCEP and chloroacetamide, and finally digested with trypsin. Extracted peptides were analyzed by LC-MS/MS and detected MS data were searched against the *Homo sapiens* database. Proteomics evaluation was carried out with the program Scaffold (MaxQuant), while protein classification was based on PANTHER-classification. Visualization of protein enrichment and depletion was performed with a Python-based script.[68] The mass spectrometry proteomics data were deposited to the ProteomeXchange Consortium via the PRIDE[69] partner repository with the dataset identifier PXD050007.

Human Seroma Liquid: Human seroma liquid was aspirated from four patients and stored at −20 °C until further use. Three patients had postoperative seroma after muscle harvesting for reconstructive purposes, while one patient underwent inguinal lymphadenectomy and had a combination of seroma and lymphocele. The clinical samples were obtained from patients who signed a general consent and were anonymized by the clinical partners. The ethics committee confirmed that no separate ethical approval was needed for the anonymized use of human seroma fluid for our study. This human seroma fluid was obtained as processed, anonymized, and ready-to-use material from the University Hospital Inselspital Bern.

Histological Samples—Rat Seroma Model: Samples from an established seroma rat model, associated with our ongoing study (Project No.: 54684.1 IP-LS), were utilized for diverse tissue analyses. In short, inbred male Lewis rats, weighing ≈200–250 g, were used for bilateral seroma induction surgery as previously outlined by our group.[35] Seromas were successfully induced by postoperative day 7, aspirated, and locally treated with CeO_2–BG hybrid NPs. At euthanasia (POD 42/End Point (EP)), seroma capsule tissue was collected for subsequent histological analyses. Serial formalin-fixed paraffin-embedded longitudinal tissue sections of skin and superficial seroma capsule tissue were then subjected to further immunohistochemistry (IHC) analyses and stained with different markers: anti-CD31/PECAM-1 (dilution 1:400; AF3628-SP, R&D Systems), representing endothelial cells, and anti-CD68 (dilution 1:200; ab125212, Abcam), representing macrophages, respectively. For the evaluation of macrophage-NP colocalization, SEM microphotographs of representative regions of CD68 stained tissue sections were digitally evaluated by labeling CD68 positive cells as one of the following cells types: individual macrophage with NPs; individual macrophage without NPs; macrophage within granuloma with NPs; macrophage within granuloma without NPs (software QuPath 0.4.3). A blinded microscopic analysis was conducted by a board-certified veterinary pathologist, Dr. Simone de Brot. The animal study adhered to the ARRIVE guidelines[70] and received approval from the Cantonal Animal Ethics Committee for Animal Experimentation, Bern, Switzerland (approval number BE 110/2020).

Protein Separation: Surface-absorbed proteins were desorbed by incubation for 15 min in 1× SDS lysis buffer at 95° C.[71] Nanoparticles were excluded from the protein-containing supernatant by centrifugation (30k ×g, 20 min). The protein concentration was determined by a detergent-compatible Bradford assay (Thermo Scientific) and adjusted with water, the 4× sample buffer, and the 10× reducing agent to a 1 mg mL^{-1} concentration (Thermo Scientific, Invitrogen Bolt Bis-Tris WPK, 15884052). 35 µL of this desorbed protein corona solution was added into an SDS-Page (12% TRIS-Bold system with 1xMEPES as a running buffer). Protein separation was performed for 20 min at 60 V, followed by 1 h at 220 V. Protein bands were visualized by Coomassie blue staining following the protocol of SimplyBlue SafeStain (Invitrogen).[71]

Nanozyme Performance—ROS Scavenging: Catalase-mimicking activity was determined based on a previously established protocol.[32] In short, nanoparticle dispersed in Ringer-lactate buffer was added into a 96-well plate, matching an H_2O_2 concentration of 50 mM with a total volume of 250 µL. Nanoparticle concentrations were used as follows, to account for activity differences: Bioglass and Ce_2O–BG Hybrid: 1 mg mL^{-1}, CeO_2: 0.25 mg mL^{-1}, Mn_3O_4: 0.02 mg mL^{-1}. After incubation for 2, 6, and 24 h, each plate was centrifuged and 200 µL of the supernatants were transferred to a glass-bottom 96 well plate (1.5 glass coverslip bottom, Cellvis) determining the H_2O_2 absorbance at 240 nm (HIDEX plate reader). Superoxide dismutase mimicking activity was determined with a commercial SOD Colorimetric Activity Kit (Invitrogen).

Nanozyme Performance—ROS Production: ROS production after X-ray irradiation was studied using a 6 MV photon beam delivering a total dose of 12 Gy with a dose rate of 6 Gy min^{-1} to the samples. 2′,7′-dichlorodihydrofluorecein diacetate (DCF-DA) powder (Sigma–Aldrich) was dissolved in dimethyl sulfoxide (DMSO, Sigma–Aldrich) at a concentration of 5 mM, followed by mixing with NaOH (10 mM) in a ratio of 1:4 to activate the solution in the dark for 30 min. Thereafter, it was diluted with Tris-HCl buffer (0.1 M, pH 7.4) to a concentration of 8 µM. The final DCF working solution was cooled and protected from light until further use. NPs were tip-sonicated in Tris-HCl buffer at 10× stock concentrations. For the irradiation experiments, 100 µL NP suspension, 100 µL Tris-HCl buffer, and 800 µL H2DCF working solution were filled into the 36 most central wells (in order to assure homogeneous dose deposition) of two transparent 96-well plates (one plate as 0 Gy reference plate, the other plate for 12 Gy irradiation). After irradiation, dispersions were centrifuged in microtubes. Triplicates of the supernatant were transferred to transparent 96-well plates. The fluorescence signal was measured using a microplate reader (485 nm excitation, 535 nm emission, Tecan infinite 200Pro or Mithras LB 943 Multimode) and referenced to the control (0 Gy) plate. ROS production after UV illumination was determined by a similar DCF assay. In short, 0.1 mg mL^{-1} NP dispersions were incubated with 8 µM DCF-DA in Tris-HCl buffer (0.1 M, pH 7.4) and illuminated via UV light (300–400 nm, Höhne Halogen lamp, black light filter, 40 mW cm^{-2} @355 nm), whereas the corresponding fluorescence signal was measured in a 96-well format (485 nm excitation, 535 nm emission, Tecan infinite 200Pro or Mithras LB 943 Multimode).

EPR Spectroscopy: EPR spectroscopy was performed by Adani-powered device spinscan X (flat cell) in combination with a peristaltic pump (Shenchen, Model LabS3). The solution of TiO_2 (1 mg mL^{-1}) was placed in a glass beaker under a UV radiation source (300–400 nm, Höhne Halogen lamp, black light filter, 40 mW cm^{-2} @355 nm) with continuous stirring and external cooling. The centerfield of the measurement was chosen to be 335 mT with 8 mT sweep width, acquiring the signal with 60 s sweep time and 25 dB attenuation for 30 min each. 5,5-Dimethyl-

1-Pyrrolin N-Oxid (DMPO, VWR) radical scavenger was added shortly before the experiment to match an overall concentration of 100 mM in Milli-Q H_2O.

Macrophage Viability and Nanoparticle Uptake: THP-1 cells were subcultured routinely in RPMI-1640 Medium (Sigma, R0883) supplemented with 10% fetal bovine serum (Sigma F9665), 1% L-glutamine (Sigma 59292C), and 1% penicillin–streptomycin–neomycin solution (Sigma P4083) at 37 °C and 5% CO_2. Macrophages were differentiated from THP-1 cells by culturing 40.000 cells per well in a 96-well with 200 nM phorbol 12-myristate 13-acetate (PMA). After 72 h, the PMA-containing cell medium was replaced by 100 µL fresh growth medium. After 2 days of equilibration, the cell medium was replaced by 80 µL fresh growth medium. Then 10 µL aqueous nanoparticle suspensions (at a concentration of 1000 µg mL^{-1}) or vehicle controls (ddH_2O) were added to the wells. The final nanoparticle concentrations were 100 µg mL^{-1} each. After 0 and 8 h of nanoparticle incubation, 10 µL H_2O_2 at the corresponding concentration was added. Due to severe Mn_3O_4 nanoparticle toxicity only in the case of 8 h nanoparticle incubation, the Mn_3O_4 nanoparticle concentration in this particular case was reduced 20 times reaching 5 µg mL^{-1}. 2 h after H_2O_2 addition, cell viability was quantified using the CellTiter-Glo assay (Promega, G7573) using a 75 µL: 75 µL ratio of CellTiter-Glo reagent to fresh cell medium. Cell viability was expressed normalized to the viability of control cells. Macrophage cell culture for CeO_2–BG hybrid uptake study was conducted in a similar way, plating $10^{[6]}$ cells per well in a six-well plate with a final NP concentration of 50 µg mL^{-1}. Detached cells were either used for Ce determination by ICP-MS or fixated, embedded, and prepared for TEM micrographs as described in the Supporting Information. TEM micrographs of *S. aureus* infected monocyte-derived macrophages were derived from experiments described previously.[62]

Statistical Analysis: Quantification of surface-absorbed proteins was carried out in three independent experiments (n = 3, mean ± SD). TEM-based NP size evaluation used the Weibull distribution of the descriptive histograms. Proteomics analysis was carried out in three independent experiments (n = 3, mean ± SD) and evaluated with principal component analysis (PCA) (ecliptic confidence interval 2σ,). Cell viability and NP uptake experiments were conducted in independent experiments (mean ± SD, $n = 3$). NP catalytic activity was accessed in three independent experiments (mean ± SD, $n = 3$). Macrophage cell viabilities was tested in independent experiments (mean ± SD, $n = 3$) and evaluated by one-way ANOVA. Software used for statistical analysis included OriginPro 2023, GraphPad Prism 10.1.0, Microsoft 365 Excel, and Scaffold 5.1.2.

Supporting Information

Supporting Information is available from the Wiley Online Library or from the author.

Acknowledgements

The authors gratefully acknowledge the help from Dr. Sibylle Pfammatter and FGCZ for the proteomic analyses and the technical support (Functional Genomics Center Zurich (FGCZ), University/ETH Zurich), as well as the help of Dr. Paul Mack (Thermo Fisher Scientific) for the XPS measurements. The authors further want to thank Sebastian Habermann for his help during TEM micrograph preparation and Theresa Göttling for her help during nanozyme ROS production evaluation. This work was supported in parts by an Innosuisse grant (Project no.: 54684.1 IP-LS, I.L. and I.K.H.), an ETH Career Seed Award funded through the ETH Zurich Foundation (R.N.), an ETH Zurich grant (no. ETH-07 21–2, I.K.H.), the Swiss Cancer Research Foundation (Grant number KFS-4868-08-2019, I.K.H.) and the Swiss National Science Foundation (Eccellenza grant no. 181290, I.K.H.).

Open access funding provided by Eidgenossische Technische Hochschule Zurich.

Conflict of Interest

M.T.M and I.K.H. declare inventorship on a patent application of ETH Zurich and Empa related to nanoparticle compositions (EP21168502). All other authors declare that they have no known competing financial interests or personal relationships that could have appeared to influence the work reported in this paper.

Author Contributions

R.N. and I.K.H. designed and conceived the research. I.K.H. coordinated the project. L.D. performed a bioinformatical analysis of the proteomics data and helped with ROS scavenging assay, A.G. helped with SEM and ICP-MS experiments, L.R.H.G performed functional macrophage assay, M.D. performed EPR spectroscopic analysis, M.Z. performed ROS production after X-ray irradiation assay, M.A.P. prepared histological rat seroma samples, A.L.N. performed macrophage viability and nanoparticle uptake experiments, M.T.M helped with initial NP synthesis and performed antibacterial intracellular activity assay, V.M.K prepared TEM micrographs, S.D.B. performed SEM-Histology correlation, I.L. supervised the rat seroma model. All other experiments were performed by R.N. All authors contributed to the manuscript writing and have given approval to the final version of the manuscript.

Data Availability Statement

The data that support the findings of this study are available from the corresponding author upon reasonable request. The mass spectrometry proteomics data have been deposited to the ProteomeXchange Consortium via the PRIDE partner repository with the dataset identifier PXD050007.

Keywords

metal oxides, nanocatalyst, nanozyme, protein corona, wound healing

Received: November 30, 2023
Revised: March 12, 2024
Published online:

[1] D. P. Cormode, L. Gao, H. Koo, *Trends Biotechnol.* **2018**, *36*, 15.
[2] S. Ahmadi, K. Rahimizadeh, A. Shafiee, N. Rabiee, S. Iravani, *Process Biochem.* **2023**, *131*, 154.
[3] A. C. Anselmo, S. Mitragotri, *Bioeng. Transl. Med.* **2019**, *4*, e10143.
[4] B. Pelaz, C. Alexiou, R. A. Alvarez-Puebla, F. Alves, A. M. Andrews, S. Ashraf, L. P. Balogh, L. Ballerini, A. Bestetti, C. Brendel, S. Bosi, M. Carril, W. C. W. Chan, C. Chen, X. Chen, X. Chen, Z. Cheng, D. Cui, J. Du, C. Dullin, A. Escudero, N. Feliu, M. Gao, M. George, Y. Gogotsi, A. Grünweller, Z. Gu, N. J. Halas, N. Hampp, R. K. Hartmann, et al., *ACS Nano* **2017**, *11*, 2313.
[5] M. T. Matter, J. H. Li, I. Lese, C. Schreiner, L. Bernard, O. Scholder, J. Hubeli, K. Keevend, E. Tsolaki, E. Bertero, S. Bertazzo, R. Zboray, R. Olariu, M. A. Constantinescu, R. Figi, I. K. Herrmann, *Adv. Sci.* **2020**, *7*, 33300.
[6] I. Lese, D. A. Graf, C. Tsai, A. Taddeo, M. T. Matter, M. A. Constantinescu, I. K. Herrmann, R. Olariu, *PLoS One* **2018**, *13*, 0207802.
[7] H. Yu, J. Peng, Y. Xu, J. Chang, H. Li, *ACS Appl. Mater. Interfaces* **2016**, *8*, 703.
[8] T. Kurahashi, J. Fujii, *J. Dev. Biol.* **2015**, *3*, 57.
[9] J. Mu, C. Li, Y. Shi, G. Liu, J. Zou, D. Y. Zhang, C. Jiang, X. Wang, L. He, P. Huang, Y. Yin, X. Chen, *Nat. Commun.* **2022**, *13*, 2513.

[10] X. Ma, B. Zhang, N. Ma, C. Liu, Y. Miao, X. Liang, S. Guan, D. Li, A. Liu, S. Zhou, *ACS Appl. Mater. Interfaces* **2022**, *15*, 13869.
[11] X. Cai, S. Seal, J. F. McGinnis, *Mol. Vision* **2016**, *22*, 1176.
[12] A. Cimini, B. Dangelo, S. Das, R. Gentile, E. Benedetti, V. Singh, A. M. Monaco, S. Santucci, S. Seal, *Acta Biomater.* **2012**, *8*, 2056.
[13] S. Jin, C. Wu, Z. Ye, Y. Ying, *Sens. Actuators, B Chem* **2019**, *283*, 18.
[14] Y. Yang, Z. Mao, W. Huang, L. Liu, J. Li, J. Li, Q. Wu, *Sci. Rep.* **2016**, *6*, 35344.
[15] Z. Shen, Q. Ma, X. Zhou, G. Zhang, G. Hao, Y. Sun, J. Cao, *NPG Asia Mater* **2021**, *13*, 39.
[16] D. Kwatra, A. Venugopal, S. Anant, *Transl Cancer Res* **2013**, *2*, 330.
[17] L. R. H. Gerken, A. Gogos, F. H. L. Starsich, H. David, M. E. Gerdes, H. Schiefer, S. Psoroulas, D. Meer, L. Plasswilm, D. C. Weber, I. K. Herrmann, *Nat. Commun.* **2022**, *13*, 3248.
[18] L. R. H. Gerken, A. L. Neuer, P. M. Gschwend, K. Keevend, A. Gogos, A. H. C. Anthis, L. Aengenheister, S. E. Pratsinis, L. Plasswilm, I. K. Herrmann, *Chem. Mater.* **2021**, *33*, 3098.
[19] M. Zimmermann, L. R. H. Gerken, S. Wee, V. M. Kissling, A. L. Neuer, E. Tsolaki, A. Gogos, M. R. Lukatskaya, I. K. Herrmann, *Biomater. Sci.* **2023**, *11*, 7826.
[20] S. Bonvalot, P. L. Rutkowski, J. Thariat, S. Carrère, A. Ducassou, M. P. Sunyach, P. Agoston, A. Hong, A. Mervoyer, M. Rastrelli, V. Moreno, R. K. Li, B. Tiangco, A. C. Herraez, A. Gronchi, L. Mangel, T. Sy-Ortin, P. Hohenberger, T. de Baère, A. Le Cesne, S. Helfre, E. Saada-Bouzid, A. Borkowska, R. Anghel, A. Co, M. Gebhart, G. Kantor, A. Montero, H. H. Loong, R. Vergés, et al., *Lancet Oncol.* **2019**, *20*, 1148.
[21] K. Reed, A. Cormack, A. Kulkarni, M. Mayton, D. Sayle, F. Klaessig, B. Stadler, *Environ. Sci.: Nano* **2014**, *1*, 390.
[22] R. N. McCormack, P. Mendez, S. Barkam, C. J. Neal, S. Das, S. Seal, *J. Phys. Chem. C* **2014**, *118*, 18992.
[23] S. Tenzer, D. Docter, J. Kuharev, A. Musyanovych, V. Fetz, R. Hecht, F. Schlenk, D. Fischer, K. Kiouptsi, C. Reinhardt, K. Landfester, H. Schild, M. Maskos, S. K. Knauer, R. H. Stauber, *Nat. Nanotechnol.* **2013**, *8*, 772.
[24] M. Mahmoudi, M. P. Landry, A. Moore, R. Coreas, *Nat. Rev. Mater.* **2023**, *8*, 422.
[25] M. P. Monopoli, C. Åberg, A. Salvati, K. A. Dawson, *Nat. Nanotechnol.* **2012**, *7*, 779.
[26] S. Tenzer, D. Docter, S. Rosfa, A. Wlodarski, J. Kuharev, A. Rekik, S. K. Knauer, C. Bantz, T. Nawroth, C. Bier, J. Sirirattanapan, W. Mann, L. Treuel, R. Zellner, M. Maskos, H. Schild, R. H. Stauber, *ACS Nano* **2011**, *5*, 7155.
[27] M. Yang, E. Wu, W. Tang, J. Qian, C. Zhan, *J. Mater. Chem. B* **2021**, *9*, 6713.
[28] D. Nierenberg, A. R. Khaled, O. Flores, *Reports Pract. Oncol. Radiother.* **2018**, *23*, 300.
[29] E. Papini, R. Tavano, F. Mancin, *Front Immunol* **2020**, *11*, 567365.
[30] R. Cagliani, F. Gatto, G. Bardi, *Materials* **2019**, *12*, 1991.
[31] X. Zhang, Y. Liu, S. Gopalakrishnan, L. Castellanos-Garcia, G. Li, M. Malassiné, I. Uddin, R. Huang, D. C. Luther, R. W. Vachet, V. M. Rotello, *ACS Nano* **2020**, *14*, 4767.
[32] M. T. Matter, L. A. Furer, F. H. L. Starsich, G. Fortunato, S. E. Pratsinis, I. K. Herrmann, *ACS Appl. Mater. Interfaces* **2019**, *11*, 2830.
[33] M. Cannio, D. Bellucci, J. A. Roether, D. N. Boccaccini, V. Cannillo, *Materials* **2021**, *14*, 5440.
[34] I. Negut, C. Ristoscu, *Appl. Sci.* **2023**, *13*, 6151. .
[35] I. Lese, C. Tsai, M. Matter, T. Wüthrich, H. S. Scheer, A. Taddeo, M. A. Constantinescu, I. K. Herrmann, R. Olariu, *ACS Biomater. Sci. Eng.* **2021**, *7*, 2676.
[36] F. Meierhofer, L. Mädler, U. Fritsching, *AIChE J.* **2020**, *66*, e16885.
[37] G. Bashiri, M. S. Padilla, K. L. Swingle, S. J. Shepherd, M. J. Mitchell, K. Wang, *Lab Chip* **2023**, *23*, 1432.
[38] Y. Li, J. S. Lee, *Materials* **2020**, *13*, 3093.
[39] S. Patil, A. Sandberg, E. Heckert, W. Self, S. Seal, *Biomaterials* **2007**, *28*, 4600.
[40] S. Panico, S. Capolla, S. Bozzer, G. Toffoli, M. Dal Bo, P. Macor, *Pharmaceutics* **2022**, *14*, 2605.
[41] F. Vianello, A. Cecconello, M. Magro, *Int. J. Mol. Sci.* **2021**, *22*, 7625.
[42] Z. Chen, X. Chen, J. Huang, J. Wang, Z. Wang, *Biomimetics* **2022**, *7*, 126.
[43] H. Mi, A. Muruganujan, X. Huang, D. Ebert, C. Mills, X. Guo, P. D. Thomas, *Nat. Protoc.* **2019**, *14*, 703.
[44] P. D. Thomas, M. J. Campbell, A. Kejariwal, H. Mi, B. Karlak, R. Daverman, K. Diemer, A. Muruganujan, A. Narechania, *Genome Res.* **2003**, *13*, 2129.
[45] S. Sheibani, K. Basu, A. Farnudi, A. Ashkarran, M. Ichikawa, J. F. Presley, K. H. Bui, M. R. Ejtehadi, H. Vali, M. Mahmoudi, *Nat. Commun.* **2021**, *12*, 573.
[46] N. Ouassil, R. L. Pinals, J. T. Del Bonis-O'Donnell, J. W. Wang, M. P. Landry, *Sci. Adv.* **2022**, *8*, abm0898.
[47] M. T. Matter, J. H. Li, I. Lese, C. Schreiner, L. Bernard, O. Scholder, J. Hubeli, K. Keevend, E. Tsolaki, E. Bertero, S. Bertazzo, R. Zboray, R. Olariu, M. A. Constantinescu, R. Figi, I. K. Herrmann, *Adv. Sci.* **2020**, *7*, 2000912.
[48] F. Zhang, P. Wang, J. Koberstein, S. Khalid, S. W. Chan, *Surf. Sci.* **2004**, *563*, 74.
[49] I. Celardo, J. Z. Pedersen, E. Traversa, L. Ghibelli, *Nanoscale* **2011**, *3*, 1411.
[50] T. Pirmohamed, J. M. Dowding, S. Singh, B. Wasserman, E. Heckert, A. S. Karakoti, J. E. S. King, S. Seal, W. T. Self, *Chem. Commun.* **2010**, *46*, 2736.
[51] V. Baldim, F. Bedioui, N. Mignet, I. Margaill, J. F. Berret, *Nanoscale* **2018**, *10*, 6971.
[52] E. Casals, T. Pfaller, A. Duschl, G. J. Oostingh, V. F. Puntes, *Small* **2011**, *7*, 3479.
[53] S. Schöttler, G. Becker, S. Winzen, T. Steinbach, K. Mohr, K. Landfester, V. Mailänder, F. R. Wurm, *Nat. Nanotechnol.* **2016**, *11*, 372.
[54] L. Shi, J. Zhang, M. Zhao, S. Tang, X. Cheng, W. Zhang, W. Li, X. Liu, H. Peng, Q. Wang, *Nanoscale* **2021**, *13*, 10748.
[55] E. Padín-González, P. Lancaster, M. Bottini, P. Gasco, L. Tran, B. Fadeel, T. Wilkins, M. P. Monopoli, *Front Bioeng Biotechnol* **2022**, *10*, 882363.
[56] J. A. Champion, S. M. Pustulka, K. Ling, S. L. Pish, *ACS Appl. Mater. Interfaces* **2020**, *12*, 48284.
[57] N. Singh, C. Marets, J. Boudon, N. Millot, L. Saviot, L. I.n Maurizi, *Nanoscale Adv.* **2021**, *3*, 1209.
[58] J&J snaps up Nanobiotix cancer radiotherapy in $2.5bn+ deal, https://pharmaphorum.com/news/jj-snaps-nanobiotix-cancer-radiotherapy-25bn-deal (accessed: March 2024).
[59] *Nanobiotix*. NBTXR3 With or Without Cetuximab in LA-HNSCC, https://clinicaltrials.gov/study/NCT04892173 (accessed: March 2024).
[60] L. Deblock, E. Goossens, R. Pokratath, K. De Buysser, J. De Roo, *JACS Au* **2022**, *2*, 711.
[61] G. Sanità, B. Carrese, A. Lamberti, *Front. Mol. Biosci.* **2020**, *7*, 587012.
[62] M. T. Matter, M. Doppegieter, A. Gogos, K. Keevend, Q. Ren, I. K. Herrmann, *Nanoscale* **2021**, *13*, 8224.
[63] A. R. Boccaccini, J. J. Blaker, *Expert Rev. Med. Devices* **2005**, *2*, 303.
[64] M. T. Matter, F. Starsich, M. Galli, M. Hilber, A. A. Schlegel, S. Bertazzo, S. E. Pratsinis, I. K. Herrmann, *Nanoscale* **2017**, *9*, 8418.
[65] F. H. L. Starsich, P. Gschwend, A. Sergeyev, R. Grange, S. E. Pratsinis, *Chem. Mater.* **2017**, *29*, 8158.
[66] B. Lin, S. Zhou, *PolyProg. Org. Coat.* **2017**, *106*, 145.

[67] M. Geppert, M. C. Hohnholt, K. Thiel, S. Nürnberger, I. Grunwald, K. Rezwan, R. Dringen, *Nanotechnology* **2011**, *22*, 145101.
[68] R. L. Pinals, D. Yang, D. J. Rosenberg, T. Chaudhary, A. R. Crothers, A. T. Iavarone, M. Hammel, M. P. Landry, *Angew. Chem., Int. Ed.* **2020**, *59*, 23668.
[69] Y. Perez-Riverol, J. Bai, C. Bandla, D. García-Seisdedos, S. Hewapathirana, S. Kamatchinathan, D. J. Kundu, A. Prakash, A. Frericks-Zipper, M. Eisenacher, M. Walzer, S. Wang, A. Brazma, J. A. Vizcaíno, *Nucleic Acids Res.* **2022**, *50*, D543.
[70] N. Percie Du Sert, V. Hurst, A. Ahluwalia, S. Alam, M. T. Avey, M. Baker, W. J. Browne, A. Clark, I. C. Cuthill, U. Dirnagl, M. Emerson, P. Garner, S. T. Holgate, D. W. Howells, N. A. Karp, S. E. Lazic, K. Lidster, C. J. MacCallum, M. MacLeod, E. J. Pearl, O. H. Petersen, F. Rawle, P. Reynolds, K. Rooney, E. S. Sena, S. D. Silberberg, T. Steckler, H. Wuerbel, *BMJ Open Sci* **2020**, *4*, 100115.
[71] D. Docter, U. Distler, W. Storck, J. Kuharev, D. Wünsch, A. Hahlbrock, S. K. Knauer, S. Tenzer, R. H. Stauber, *Nat. Protoc.* **2014**, *9*, 2030.